Electronic Supplementary Material (ESI) for Energy & Environmental Science. This journal is © The Royal Society of Chemistry 2023

Electronic Supplementary Material (ESI) for Energy & Environmental Science.

Supplementary Information for

# Prolongating Cycling Lifetime of Lithium Metal Batteries with Monolithic and Inorganic-Rich Solid Electrolyte Interphase

Jinlin Yang[a*‡], Menghao Li[b, c‡], Zejun Sun[a‡], Xu Lian[a], Yanan Wang[d], Yuxiang Niu[a], Chonglai Jiang[a, e], Yani Luo[a, e], Yuan Liu[a, e], Zhangliu Tian[a], Yu Long[a, e], Kun Zhang[a], Pengcheng Yu[a, f], Jia Zhang[g], Zeheng Wang[h], Gang Wu[g*], Meng Gu[c*], Wei Chen[a, d, e*]

*a. Department of Chemistry, National University of Singapore, 3 Science Drive 3, 117543, Singapore*
*E-mail: yjlchem@nus.edu.sg (or yangjinlin@u.nus.edu), phycw@nus.edu.sg*
*b. School of Materials Science and Engineering, Harbin Institute of Technology, Harbin, 150001, China*
*c. Department of Materials Science and Engineering, Southern University of Science and Technology, Shenzhen 518055, China*
*E-mail: gum@sustech.edu.cn*
*d. Department of Physics, National University of Singapore, 2 Science Drive 3, 117542, Singapore*
*e. Joint School of National University of Singapore and Tianjin University, International Campus of Tianjin University, Binhai New City, Fuzhou, 350207, P. R. China*
*f. Academy for Advanced Interdisciplinary Studies, Southern University of Science and Technology, Shenzhen 518055, China*
*g. Institute of High-Performance Computing, Agency for Science, Technology and Research, 1 Fusionopolis Way, #16-16 Connexis, Singapore 138632, Singapore*
*E-mail: wug@ihpc.a-star.edu.sg*
*h. School of Electrical Engineering and Telecommunications, The University of New South Wales, Sydney, NSW 2052, Australia*
[‡] These authors contributed equally to this work.

## Experimental Procedures

**Materials.** Electrolytes were prepared in an Ar-filled glove box (Vigor Pte Ltd), in which both the content of $O_2$ and $H_2O$ were lower than 0.5 ppm. 50 or 100 µm Li was obtained via electric roller in our lab and lithium iron phosphate ($LiFePO_4$, LFP) cathodes were purchased from Guangdong Canrd New Energy Technology Co.,Ltd., China. The solvents, 1,2-dimethoxyethane (DME, anhydrous, 99.5%, inhibitor-free, Sigma-Aldrich) and 1,3-dioxolane (DOL, anhydrous, contains ~75 ppm BHT as inhibitor, 99.8%, Sigma-Aldrich), were further dried with 4 Å molecular sieve. The salts, lithium bis(trifluoromethanesulfonyl)imide (LiTFSI, 99.95% trace metals basis, Sigma-Aldrich), lithium nitrate ($LiNO_3$, 99.99% metal basis, Sigma-Aldrich), potassium methoxide ($CH_3OK$, 95%, Sigma-Aldrich), sodium methoxide ($CH_3ONa$, 95%, Sigma-Aldrich), lithium methoxide ($CH_3OLi$, 98%, Sigma-Aldrich) were used. LiTFSI was vacuum dried at 120 °C overnight and other salts were used directly without further purification. Electrolyte, 2wt% $LiNO_3$ and 1 M LiTFSI were dissolved in DME and DOL with a volume ratio of 1:1, denoted as blank electrolyte. Additional 0.04 M $CH_3OK$ in the blank electrolyte was denoted as modified electrolyte. All the electrolytes were magnetically stirred to obtain homogeneous suspension solution.

**Electrochemical Characterizations.** 2032-type coin-cell batteries were assembled in a glovebox. Li|Cu asymmetric electrochemical cells were assembled with the thick lithium foil (600 µm) as the anode (diameter, 10 mm), the Cu foil as the counter electrode (diameter, 16mm), and the Celgard 2325 as the separator. The amount of electrolyte was 40 µl. To assemble the full-cell batteries with an N/P ratio of ~6 or 3, the commercial Li metal was electrically rolled to 50 µm and then paired with the $LiFePO_4$ cathode with a mass loading of ~10.5 or 20 mg $cm^{-2}$. $LiFePO_4$|Li batteries were assembled with thin Li foil (50 µm) as anode, $LiFePO_4$ with a mass loading of ~ 10.5 or 20 mg $cm^{-2}$ as the cathode and a electrolyte of 10 uL/mAh. All electrochemical batteries were performed on Land or Neware battery testers. The EIS, and CV measurements were carried out on an AUTOLAB electrochemical workstation. CV profiles were obtained in a voltage window of 2.5 V to -0.1 V or 0.3 to -0.1 V for the asymmetrical Li-Cu cells. The temperature-dependent EIS spectra were collected in a symmetric cell of Li|Li with the blank or the modified electrolyte at a plated state with a frequency range of $10^5$ Hz–0.01 Hz and an AC voltage amplitude of 10 mV. Differential capacitance-potential (DCP) curves were calculated from alternating current voltammetry (ACV) results. In the ACV tests, the applied frequency is 1000 Hz with an amplitude of 5 mV in a voltage range of -0.35V~0.35V at a scan rate of 10 mV $s^{-1}$. The capacitance can be calculated by the following formulas:[1]

$$\emptyset = tan^{-1}\frac{i_{90}}{i_0}$$

$$Z = \frac{A}{\sqrt{i_{90}^2 + i_0^2}}$$

$$Z_{Re} = Z\cos a?\ldots$$

$$Z_{Im} = Z\sin a?\ldots$$

$$C = \frac{1}{?\%_0 Z_{Im}}$$

Where $a?\ldots$ is the phase shift, $i_0$ and $i_{90}$ are the currents at phase angles of 0° and 90°, respectively, A is the applied voltage, $Z_{Re}$ and $Z_{Im}$ are the real and imaginary parts of the impedance, C is the interfacial capacitance.

**Physical Characterizations.** SEM images were obtained by a JEOL JSM-6701F FESEM. Raman spectroscopy and spatial mapping were recorded at room temperature using a confocal WiTec Alpha 300R with laser excitation at 532 nm. A small amount of the deposit of 0.5 mAh $cm^{-2}$ was plated on the Cu electrode with a current density of 0.5 mA $cm^{-2}$. The acquisition time for each Raman spectrum was 30s during the Li plating process. AFM measurements were conducted on Brucker Fastscan. To prepare the samples for AFM measurements, Li|Cu cells with the blank and the modified electrolyte were assembled. Then Li with a capacity of 1 mAh $cm^{-2}$ was deposited on the Cu at a current density of 0.5 mA $cm^{-2}$. Before Li plating, the cells with the blank and the modified electrolyte were cycled twice from 0 to 2.5 V at a current density of 0.05 mA $cm^{-2}$ for interface activation and stabilization. XPS spectra were collected using an Omicron EA125 system with Al Kα (1486.7 eV) X-ray source. A home-built vacuum transfer chamber was implemented for transferring the samples from glovebox into XPS chamber to avoid degradation toward air. The sputtering was conducted using an Argon ion sputtering gun with operation energy of 1.0 KeV at Argon pressure of $5.0\times10^{-5}$ mbar. The sputtering rate is about 1.5 ± 0.5 nm/min, depending on the composition and structure of the samples. Hence, the sputtering thickness in 20 minutes is about 30 ± 10 nm. All TEM characterizations were carried out using an aberration-corrected Titan Krios TEM operated at 300 kV. All cryo-TEM images were acquired at low temperature (77 K) under low dose condition (~7-10 $e{\cdot}Å^{-2}{\cdot}s^{-1}$ × 10 s at counting model for high-resolution TEM imaging) using a Falcon 3 camera.

**Computational details of molecular dynamics (MD) simulation.** In this work, MD simulations were performed using the large-scale atomic/molecular massively parallel simulator (LAMMPS). [2, 3] The condensed-phase optimized molecular potentials for atomistic simulation studies (COMPASS) force field was used to describe the bonded and nonbonded interactions. [4, 5] Long range electrostatic interactions were treated with particle-particle particle-mesh (PPPM) method. [6, 7] A time step of 1.0 fs was used throughout all the

simulations. Periodic boundary conditions were applied to all directions to mimic an infinite system. The Nose-Hoover thermostat and barostat were employed to maintain the desired temperature and pressure. Two electrolyte models with the different components were constructed to assess the role of methoxide molecules in regulating the solvation shell. One model consisted of 4 $CH_3OK$, 629.6 DOL, 420 DME, 40 $LiNO_3$ and 100 LiTFSI molecules according to the experimental conditions (1 M LiTFSI with 2 wt% $LiNO_3$ in 1:1 (v/v) DME and DOL, and 0.04 M $CH_3OK$ as additives), and the other model contained similar compositions except for methoxide. Three different configurations were generated for each model for better ensemble averaging. Meanwhile, two other simulation models containing lithium electrodes were constructed correspondingly. After packing the specific numbers of molecules into the simulation box using Monte-Carlo method, a multi-stage equilibration protocol was performed to compress the system to the target density while relaxing the internal stress. [8] Then, a 20-ns equilibration stage was performed in the isothermal-isobaric ensemble (NPT) at 300 K and 1 atm. The density of the electrolyte was calculated to be 1.148±0.003 g $cm^{-3}$, which agrees well with the experimental value of 1.135 g $cm^{-3}$. After obtaining the equilibrated atomic models of the electrolyte models described above, a lithium slab was inserted into the models to study the spatial distributions of the various molecules. Since we still adopted the periodic boundary conditions, the electrolyte was actually confined between two lithium electrodes. The thickness of the lithium electrode was 19.85 Å with its (110) surface facing to the electrolyte. For simplicity, the interaction between the lithium electrode and the electrolyte was assumed to be purely non-bonded, and the lithium electrode was frozen throughout the MD simulations. Finally, all the systems were further maintained in the canonical ensemble (NVT) for 50 ns during the production stage, where the radial distribution functions (RDFs) were sampled according to the trajectories to identify the intermolecular interaction pattern.

During the construction of our atomic models, the lithium ion and metal lithium atoms were identified. However, as we did not consider the reaction between the lithium anode and the electrolyte, all metal lithium atoms in the anode were kept frozen during the MD simulations. This made it straightforward to distinguish them from the $Li^+$ ions in the electrolyte. Since no bonds were formed during the MD simulation, all the atoms in the electrolyte maintained a minimum distance of 2.5 Angstroms from the anode surface, roughly equivalent to the van der Waals distance (**Figure 1a and 1b**). Besides, only small number of $Li^0$ atoms are on the surface of the Li slab, while most $Li^0$ atoms are immersed in the bulk region of the slab. As a result, the RDF of the central $Li^0$ atoms with the atoms in electrolyte always appear at a large distance, and these RDFs converge only after a significant distance (more than half the thickness of the Li slab), when the Li atoms in the bulk can 'see' the electrolyte. Noteworthy is that the deposition of $Li^+$ ions was not considered on the Li slab since no reactions were included in our simulations. Therefore, it was unnecessary to define the distance at which the $Li^+$ ions were classified as adsorbed ions. Besides, the MD simulations were performed using a classical force field, and hence, we did not need a basis set as in other first-principles simulations. Regarding the "unstable" $K^+$ solvent structure in the bulk electrolyte of the modified electrolyte, it was believed that they were referring to the roughness of the small noises in the RDF curves. The molar ratio of $CH_3OK$ was quite small in our atomic models of the electrolyte, with only 4 $CH_3OK$ molecules contributing 4 $K^+$ ions, while the entire system contained 18,462 atoms. Despite a total simulation duration of 50 ns and ensemble averaging over 4 configurations, the RDF curves for $K^+$ ions were still rough compared to other particles. Nevertheless, these RDF curves are adequate for uncovering the underlying mechanism satisfactorily.

**Density Functional theory (DFT) calculation details.** The DFT calculations were performed utilizing Gaussian 16 software package, [9] which employed Becke's three-parameter hybrid method utilizing the Lee-Yang-Parr correlation functional (B3LYP) at def2-TZVP level. [10, 11] In order to account for the solvation effect, the implicit solvation model based on density (SMD) was incorporated. [12] The solvent parameters were sourced from a previously published article. [13] Furthermore, the D3 version of Grimme's dispersion with the original D3 damping function was additionally considered in the calculations. [14]

## Results and Discussion

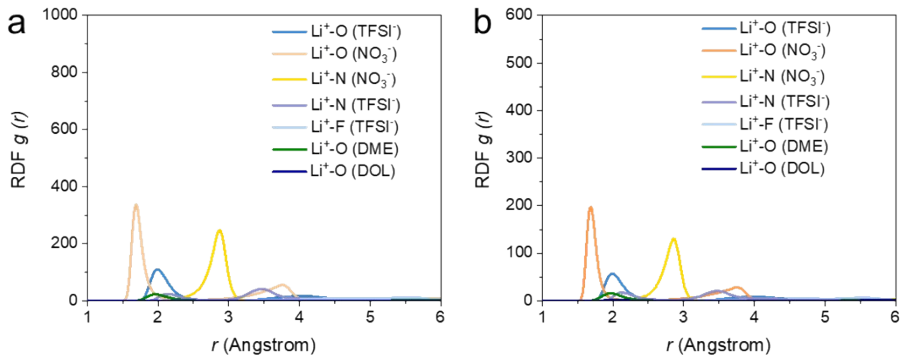


**Figure S1.** The calculated radial distribution functions RDFs of $Li^+$ in the blank electrolyte (a) near Li slab and (b) bulk electrolyte.

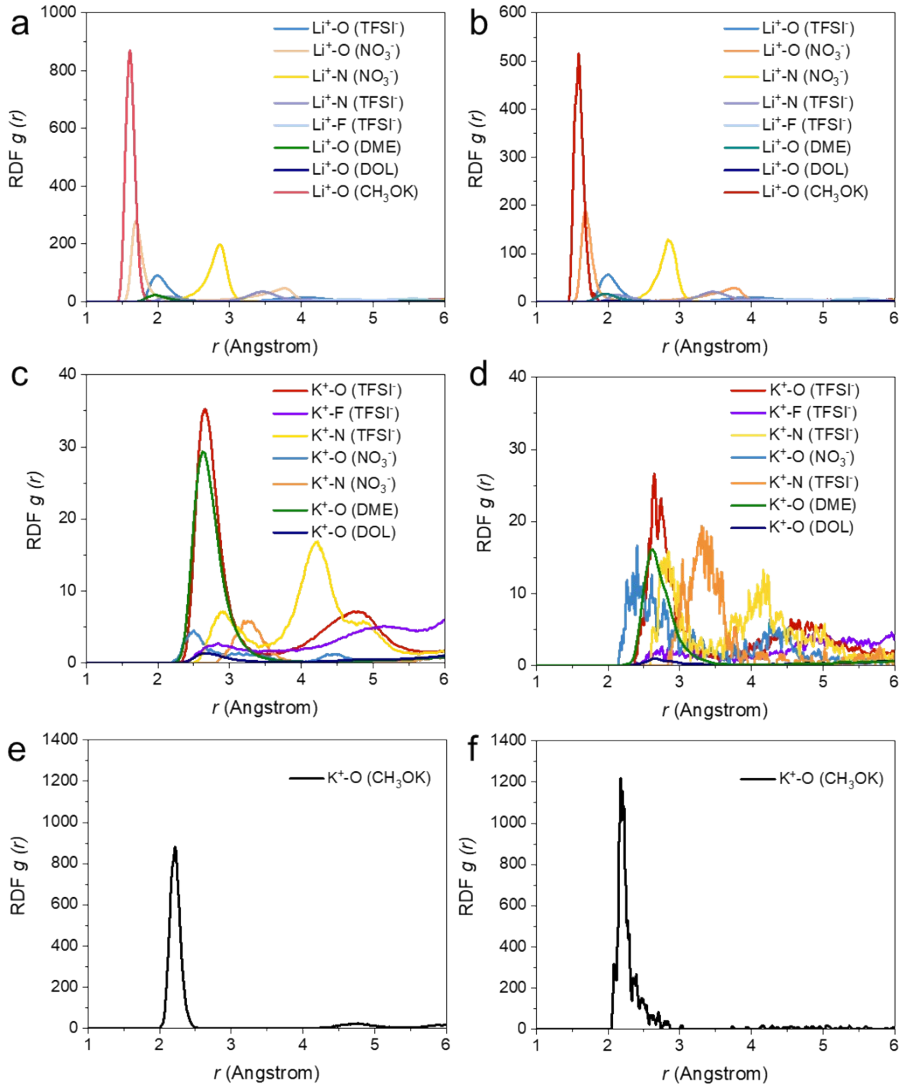


**Figure S2.** The calculated radial distribution functions (RDFs) of $Li^+$ (a) near Li slab and (b) in bulk electrolyte and of $K^+$ (c,e) near Li slab and (d, f) in bulk electrolyte of the modified electrolyte.

**Notes:** The strong interaction between $CH_3O^-$ and $Li^+$ can be observed near Li slab and in bulk electrolyte of the modified electrolyte. Besides, as can be seen in **Figure S1** and **S2,** the solvent molecules in the $Li^+$ solvation structure are mainly DME molecules and nearly no DOL molecules can be observed, which can be attributed to the weak solvating capability of DOL molecules.

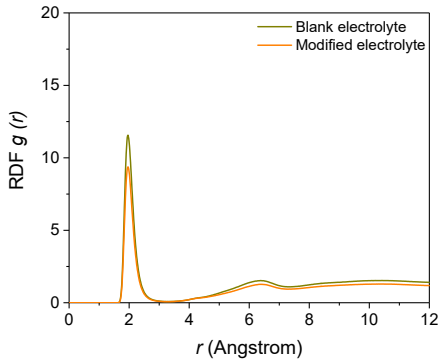


**Figure S3.** The calculated radial distribution functions (RDFs) of $Li^+$-O (DME & DOL) near Li slab in the blank and the modified electrolyte.

**Notes:** The methoxide anions ($CH_3O^-$) preferentially participate in the $Li^+$ solvation structure, weakening the cation-solvent interaction.

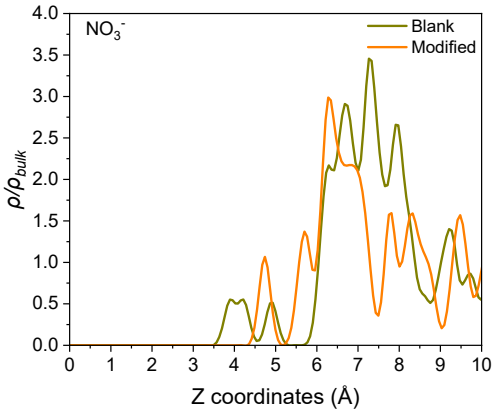


**Figure S4.** MD-obtained normalized number density profiles of $NO_3^-$ at the Li-metal surface in the blank electrolyte and modified electrolyte.

**Notes:** To disclose the effect of $CH_3OK$ additive on the distribution of $LiNO_3$, the normalized number density profiles (i.e., number density normalized by the bulk density) of $NO_3^-$ at the Li-metal surface in the blank electrolyte and modified electrolyte were plotted out for comparison. As can be seen in **Figure S4**, the $NO_3^-$ anions in the modified electrolyte accumulate at the distance between 4.5 and 7 Å away from Li slab while those in the blank electrolyte mainly accumulate at the distance between 6 and 8.5 Å away from Li slab. The closer distance between $NO_3^-$ anions and Li slab in the modified electrolyte make them more easily be decomposed in the modified electrolyte than in the blank electrolyte.

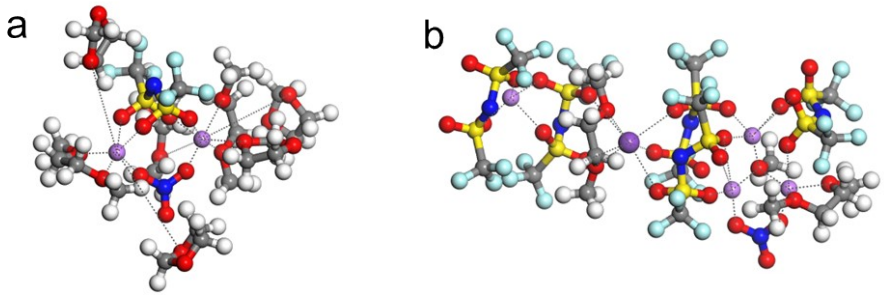


**Figure S5.** Representative configurations of the solvation structures of $Li^+$ in (a) the blank and (b) the modified electrolyte. (H: white, O: red, C: grey, N: blue, S: yellow, F: light blue, $Li^+$: light purple, $K^+$: dark purple.)

**Notes:** As can be seen in **Figure S5**, $CH_3O^-$, functioning as a "bridging" anion, interacts with three cations at the same time, reducing the interaction between solvent and cations and increasing the proportion of AGGs and CIPs. As regards the "bridge" characteristics of $CH_3OK$, it will be more accurate to be described as aggregates (AGGs), meaning one anion interacts with more than one cation at the same time.

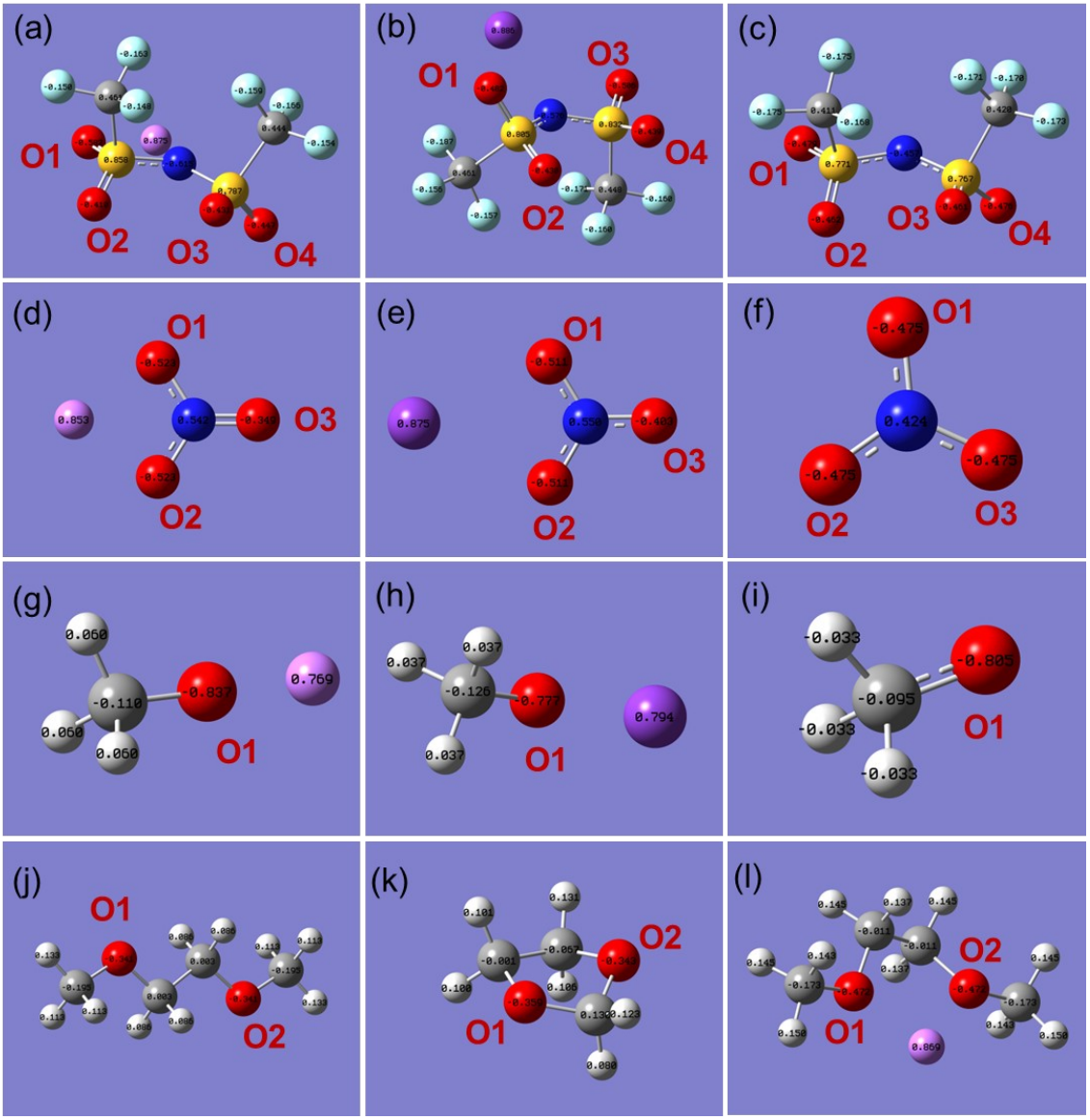


**Figure S6.** Structural properties of (a) LiTFSI, (b) KTFSI, (c) $TFSI^-$, (d) $LiNO_3$, (e) $KNO_3$, (f) $NO_3^-$, (g) $CH_3OLi$, (h) $CH_3OK$, (i) $CH_3O^-$, (j) DME, (k) DOL, and (l) DME-$Li^+$. (H: white, O: red, C: grey, N: blue, S: yellow, F: light blue, $Li^+$: light purple, $K^+$: dark purple.)

**Notes:** Electronegativity has a great influence on the binding ability of one specific atom with $Li^+$. Hence, the Mulliken atomic charge of each atom in each molecule (i.e., DME, DOL, LiTFSI, $LiNO_3$, $CH_3OK$) was calculated and compared via density functional theory (DFT) calculation. As can be seen in **Table S1** and **Figure S6,** the Mulliken atomic charge of oxygen in the $CH_3O^-$ anions is much more negative than all the oxygen atoms in DME, DOL, $TFSI^-$ anions, and $NO_3^-$ anions, indicating the stronger ability of the $CH_3O^-$ anions to bound with $Li^+$ cations.

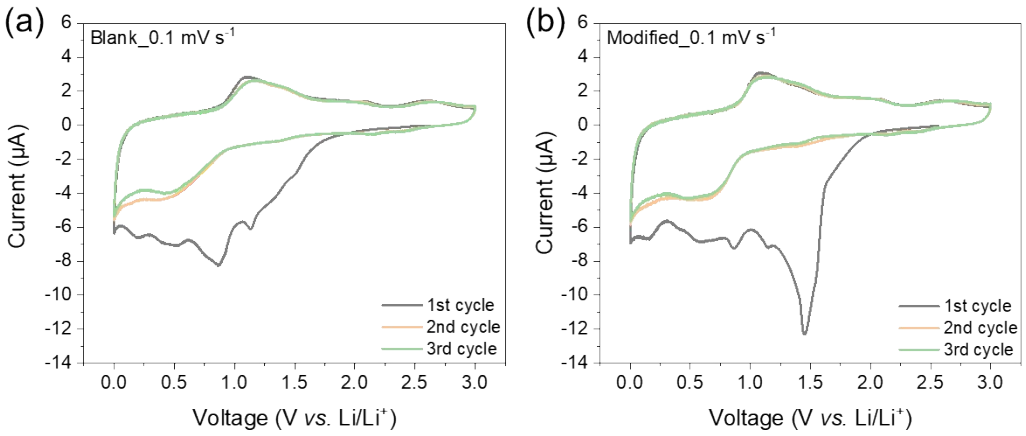


**Figure S7.** CV profiles of the asymmetric cells of Li-Cu cell with the blank and the modified electrolyte collected at 0.1 mV $s^{-1}$ in a voltage range from 3 to 0 V vs. $Li/Li^+$.

**Notes:** As can be seen in **Figure S7a**, in the first-cycle CV scanning, a drop decrement of the reduction current takes place from 1.75 V (vs. $Li/Li^+$) in the blank electrolyte. On the contrary, the reduction currents at the voltage range of 1.75V to 1 V (vs. $Li/Li^+$) nearly keep constant in the following two cycles, indicating no further decomposition of anions (i.e., $TFSI^-$ and $NO_3^-$). Hence, the broad peaks located between 1.75 and 1.25 V (vs. $Li/Li^+$) resulting from the rapid decrement of the reduction current can be attributed to the slow and continuous decomposition of $LiNO_3$ in the blank electrolyte. Besides, the profiles in **Figure 1f** are parts of CV curves collected from the blank and the modified electrolyte. As can be seen from **Figure S7**, the decomposition of the solvents and the salts mainly takes place in the first cycle CV scanning. The CV curves collected in the subsequent two cycles overlap well, indicating the decomposition of the solvents and salts is not continuous.

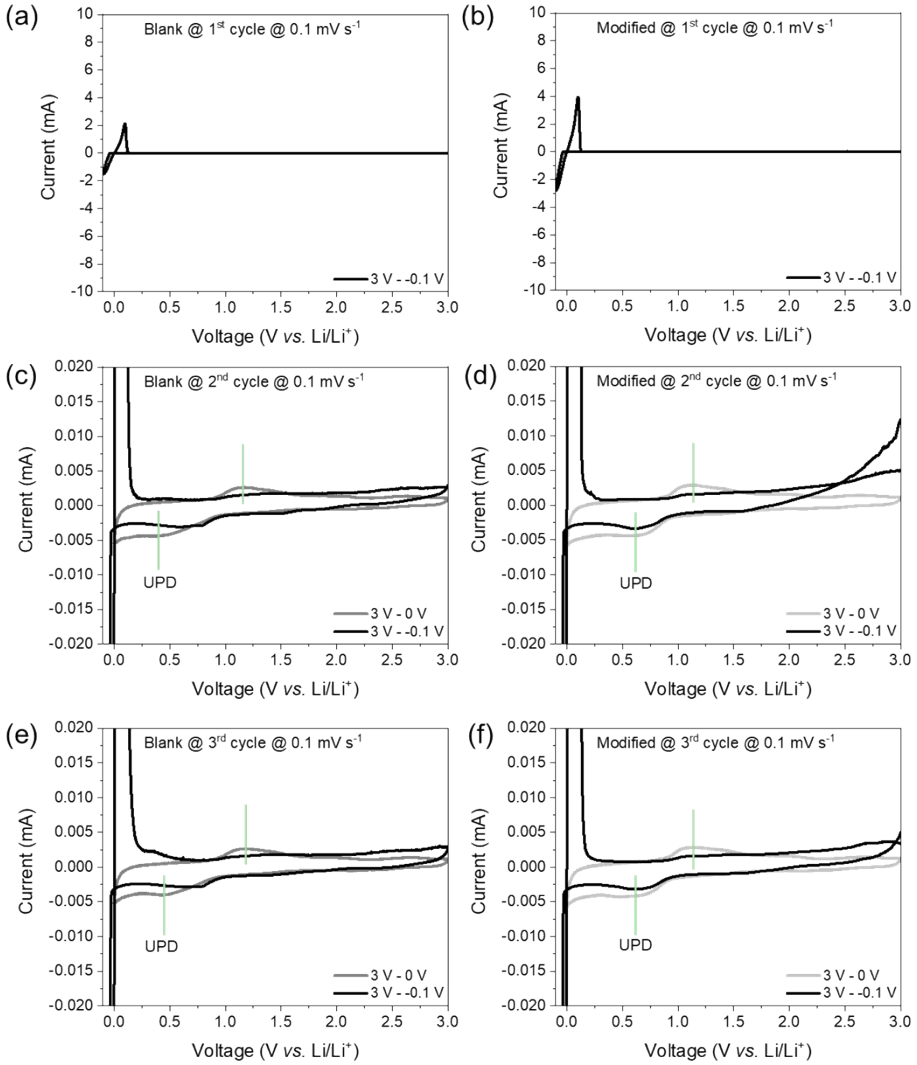


**Figure S8.** First CV scanning curves at the voltage range of 3- (-0.1) V (vs. $Li/Li^+$) in (a) the blank and (b) the modified electrolyte. Comparison of subsequent two CV scans between 3 - 0 V and 3- (-0.1) V (vs. $Li/Li^+$) in (c, e) the blank electrolyte and (d, f) the modified electrolyte. (UPD: underpotential deposition)

**Notes:** CV scans between 3-0 V and 3-(-0.1) V (vs. $Li/Li^+$) were also collected and compared to disclose the effects of the presence of the deposited Li on SEI formations. As shown in **Figure S8**, no decomposition of anions can be observed after the first CV scanning in the blank and the modified electrolyte. Besides, compared to the CV curves collected at the voltage range of 3 to 0 V (vs. $Li/Li^+$), the CV curves at the range of 3 to -0.1 V (vs. $Li/Li^+$) display obvious reduction of the underpotential deposition (UPD) peaks, indicating that the presence of the deposited Li changes the surface environment and influence the subsequent deposition. Moreover, the UPD voltages are different in the blank (~0.4 V vs. $Li/Li^+$) and the modified electrolyte (~0.6 V vs. $Li/Li^+$), further revealing the different ion absorption behaviours in the two electrolytes. [15] Noteworthy is that a small peak corresponding to the decomposition peak of the solvent can still be observed at about 0.8 V (vs. $Li/Li^+$) in the blank electrolyte with the presence of the deposited Li, indicating the porous structure of the deposited Li in the blank electrolyte.

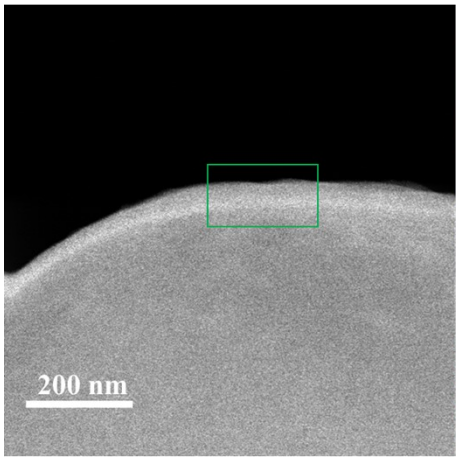


**Figure S9.** Cryo-HAADF-STEM image of Li dendrites in the modified electrolyte.

**Notes:** The region in the green box was selected to conduct electron energy loss spectroscopy (EELS) elemental maps as shown in Figure 2k in the main text.

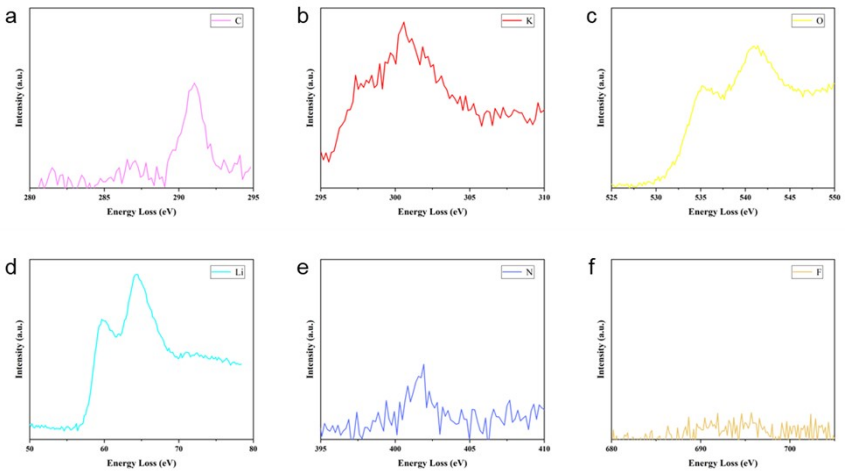


**Figure S10.** EELS spectrum of (a) C, (b) K, (c) O, (d) Li, (e) N, and (f) F in the SEI formed in the modified electrolyte.

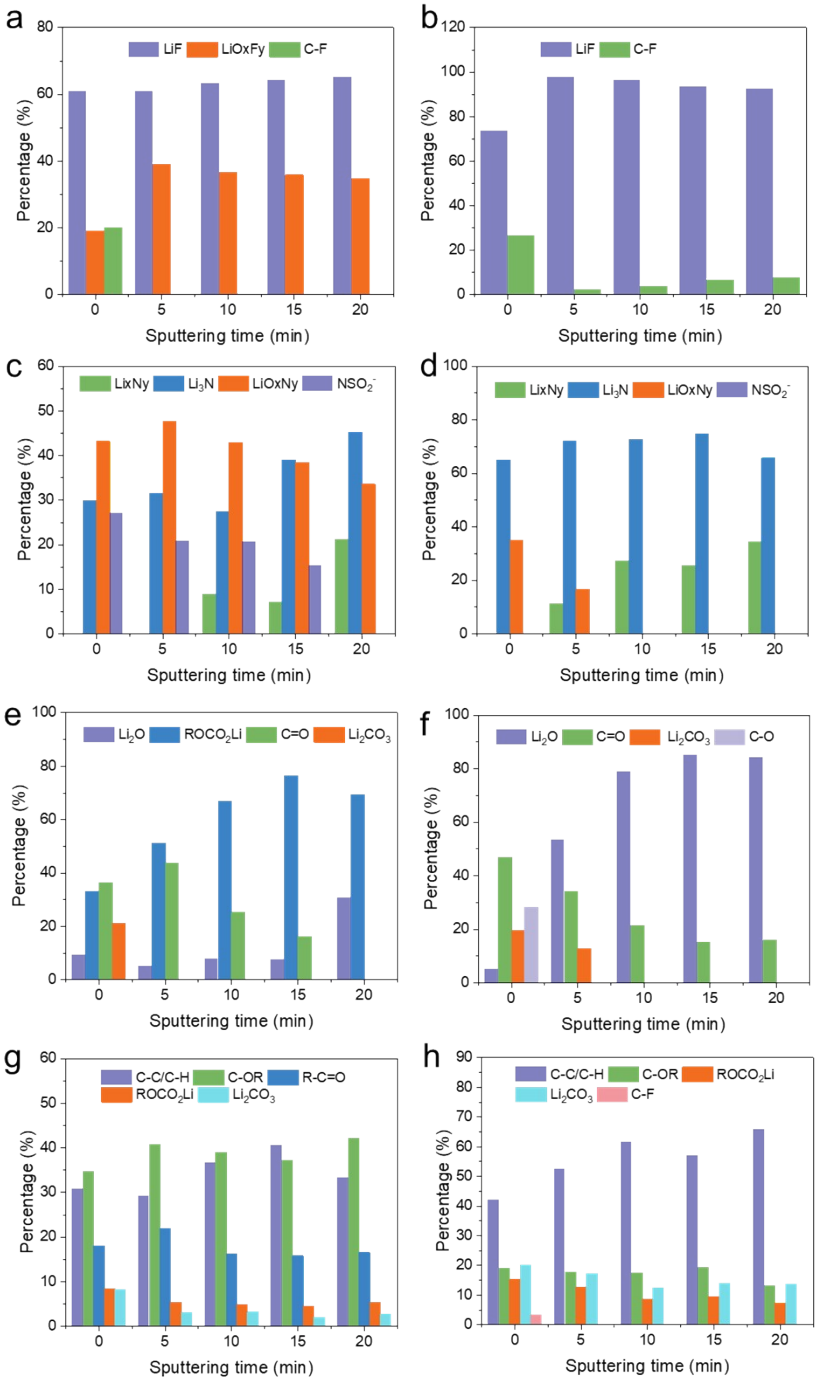


**Figure S11.** Atomic content and relative percent of the specific species in (a, b) F, (c, d) N, (e, f) O and (g, h) C XPS spectra of the samples collected from the blank and the modified electrolyte, respectively.

**Notes:** For comparison of the stability of the SEI formed in the blank electrolyte and the modified electrolyte, the atomic content, and the relative percent of the specific species in C, N, O and F XPS spectra were collected (**Figure S11**). As can be seen from Figure R5b, R5d, R5f and R5h, the SEI formed in the modified electrolyte is dominated by LiF, $Li_3N$, and $Li_2O$. These inorganic species display high Young's modulus, [16-18] contributing to the high stability of the SEI layer. Comparatively, plenty of organic species, e.g., $ROCO_2Li$, C-OR, R-C=O, can be found in the SEI layer formed in the blank electrolyte. These organic species display a much lower Young's modulus than inorganic species (e.g., LiF, $Li_3N$, and $Li_2O$) and a much higher solubility. [18] Therefore, the stability of the SEI formed in the modified electrolyte is bound to be much higher than the SEI in the blank electrolyte.

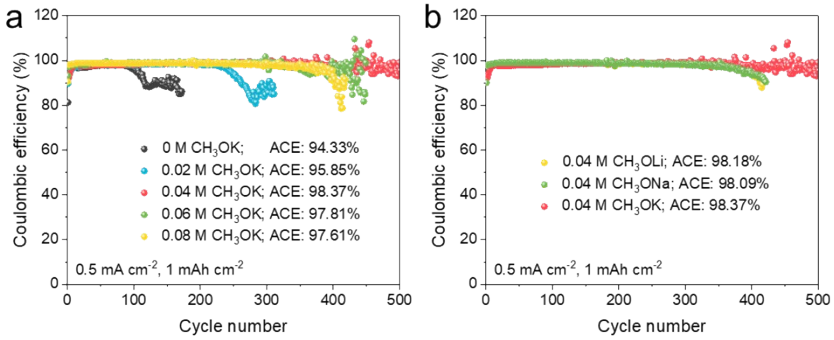


**Figure S12.** Comparison of the Coulombic efficiencies of Li plating/stripping for Li-Cu half-cells with a cycling capacity of 1 mAh $cm^{-2}$ at 0.5 mA $cm^{-2}$ in (a) blank, 0.02M $CH_3OK$-added, 0.04M $CH_3OK$-added, 0.06M $CH_3OK$-added, and 0.08M $CH_3OK$-added electrolyte and (b) 0.04M $CH_3OLi$-added, 0.04M $CH_3ONa$-added, and 0.04M $CH_3OK$-added electrolyte.

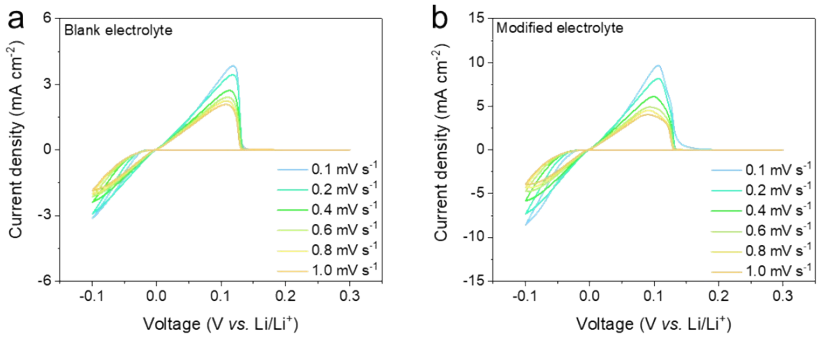


**Figure S13.** CV curves at different scan rates from 0.1 to 1 mV $s^{-1}$ in (a) the blank electrolyte and (b) the modified electrolyte.

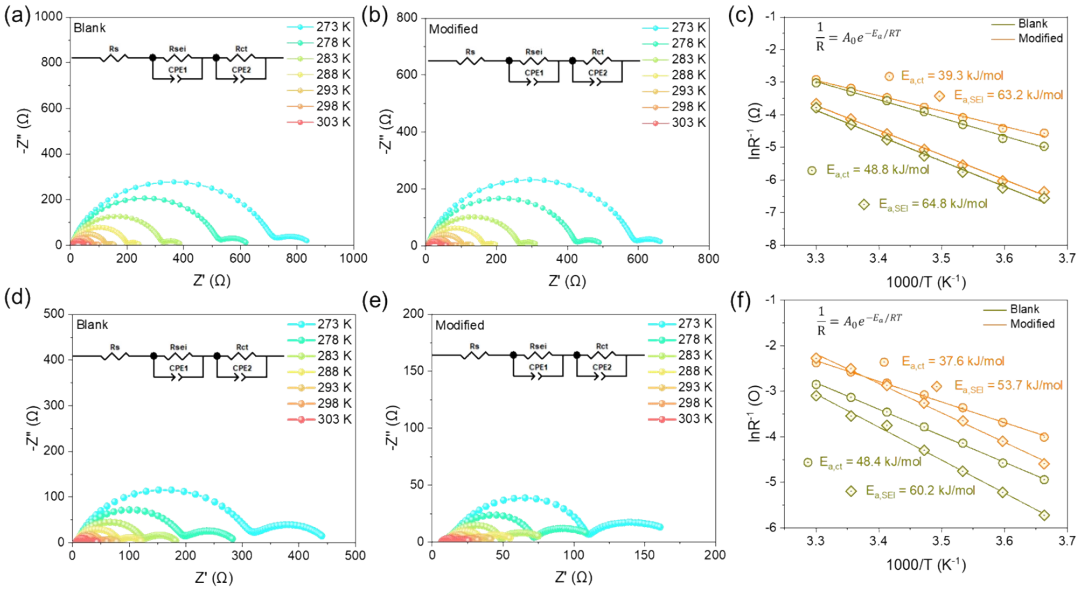


**Figure S14.** EIS spectra for various temperatures from 0 to 30 °C and comparison of the Ea values for $Li^+$ de-solvation near the SEI surface and $Li^+$ diffusion through the SEI in the corresponding electrolyte (a-c) before cycling and (d-f) after cycling.

**Notes:** The aging time for the EIS stabilization is 1 hour. To disclose the difference between chemical reactions and electrochemical reactions during the SEI formation, the temperature-dependent EIS and calculated $E_a$ were compared for cells before and after cycling. As can be seen in **Figure S14c** and **S14f**, no matter before or after cycling, the $E_{a,\,ct}$ and $E_{a,\,SEI}$ calculated from the modified

electrolyte are lower than those calculated from the blank electrolyte, indicating the improved kinetics in the modified electrolyte. Besides, the $E_{a,SEI}$ and $E_{a,ct}$ values calculated from the cells after cycling are smaller than those calculated from the cells before cycling in both two electrolytes, indicating that electrochemical reactions are more effective to fabricate a stable SEI layer than chemical reactions.

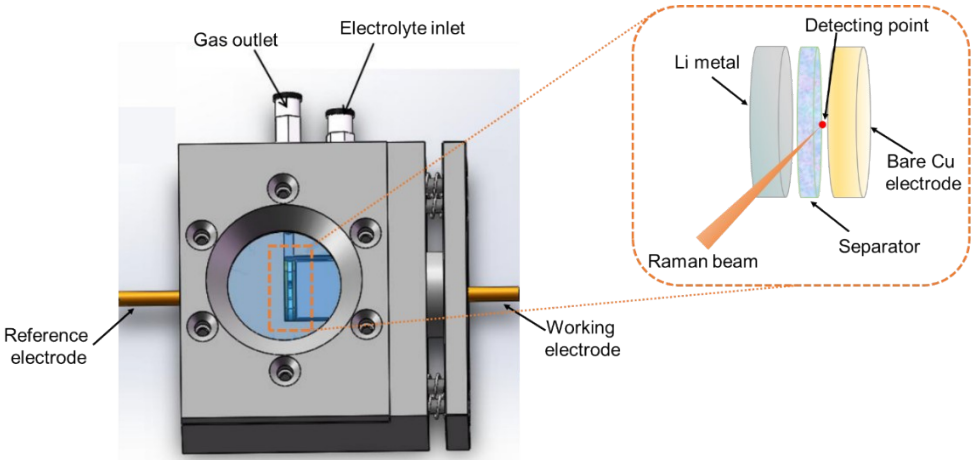


**Figure S15.** Schematic diagram about the set-up of the *in-situ* Raman measurement.

**Notes:** The Raman beam was perpendicular to the optical glass window of the *in-situ* cell (**Figure S15**) and focused on the electrolyte near the Cu foil. A small amount of the deposit of 0.5 mAh $cm^{-2}$ was plated on the Cu electrode with a current density of 0.5 mA $cm^{-2}$. The acquisition time for each Raman spectrum was 30s during the Li plating process. The *in-situ* cell was purchased from Beijing Science Star Technology Co. Ltd.

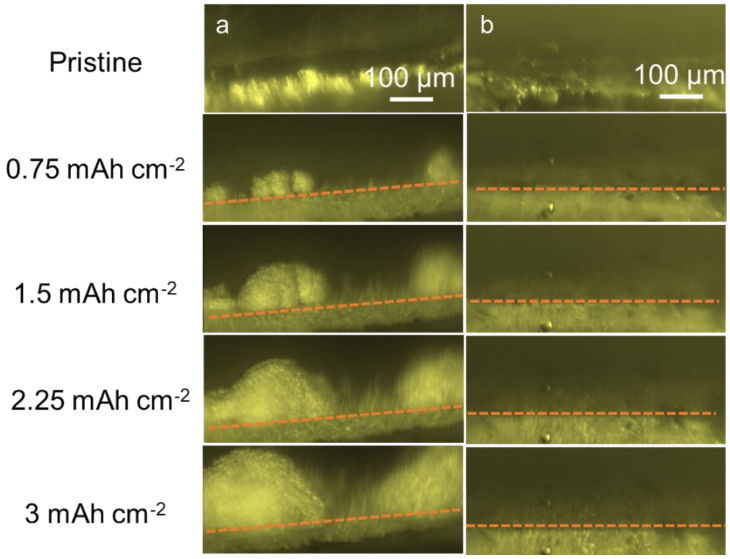


**Figure S16.** Optical microscopy observations of Li electrochemical deposition in (a) the blank electrolyte and (b) the modified electrolytes at a current density of 1.5 mA $cm^{-2}$ with a deposited capacity of 3 mAh $cm^{-2}$.

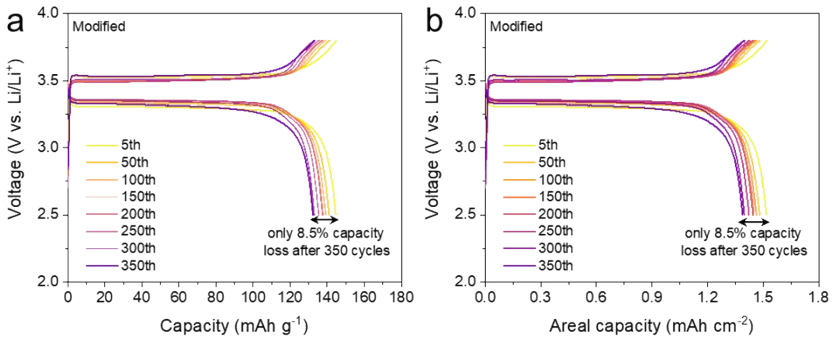


**Figure S17.** Charge/discharge curves of Li|LFP full cells in a electrolyte of 10 uL/mAh with a N/P ratio of ~6, and a LFP mass loading of ~10.5 mg $cm^{-2}$ at various cycles.

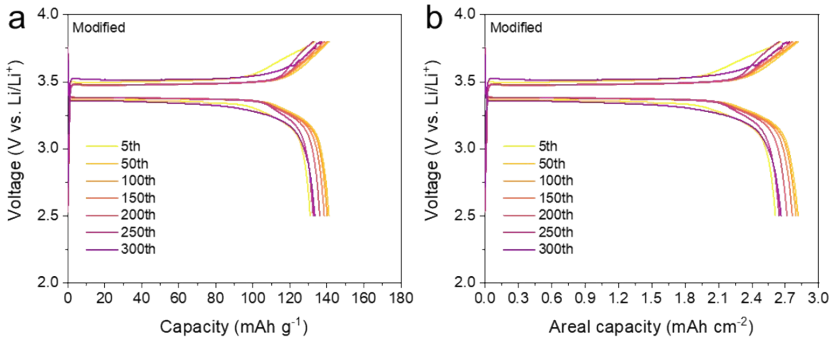


**Figure S18.** Charge/discharge curves of Li|LFP full cells in an electrolyte of 10 uL/mAh with a N/P ratio of ~3, and a LFP mass loading of ~20 mg $cm^{-2}$ at various cycles.

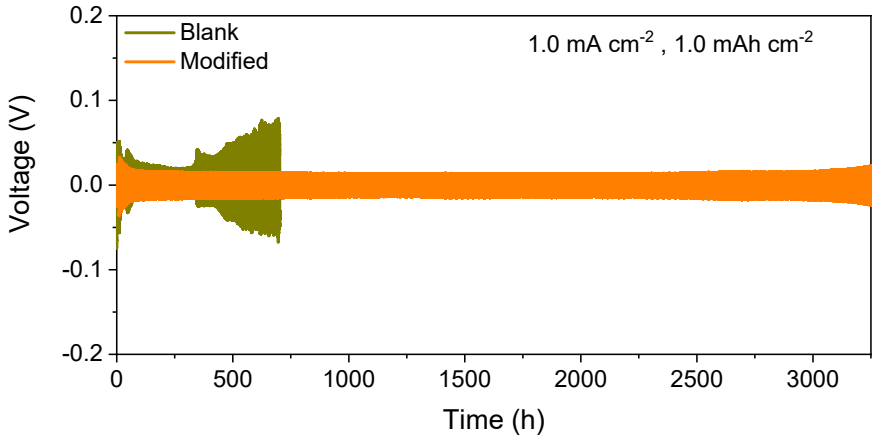


**Figure S19.** Comparison of cycling stability of Li | Li symmetric cells at a current density of 1 mA cm$^{-2}$ for 1h.

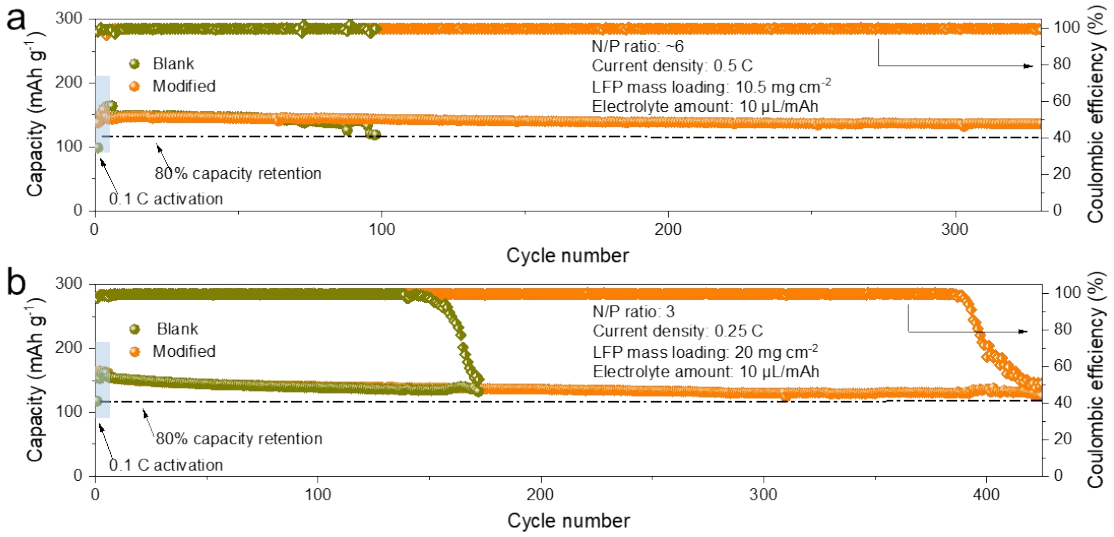


**Figure S20.** The cycling performance of Li | LFP full cells with (a) an N/P ratio of ~6, and a LFP mass loading of ~10.5 mg cm$^{-2}$ and (b) an N/P ratio of ~3, and an LFP mass loading of ~20 mg cm$^{-2}$.

**Notes:** In order to demonstrate the reproducibility of the performance variation amongst cells, one more set of the electrochemical results of the symmetric cells and full-cell batteries has been provided. As shown in Figure S19 and S20, the performance variation in the repeated experiment displays the same tendency with the results in the main text, demonstrating the good reproducibility.

**Table S1.** The Mulliken atomic charge of each oxygen atom in each molecule

| Molecule \ Atom | O1 | O2 | O3 | O4 |
|---|---|---|---|---|
| LiTFSI | -0.582 | -0.410 | -0.431 | -0.447 |
| KTFSI | -0.482 | -0.438 | -0.506 | -0.439 |
| $TFSI^-$ | -0.479 | -0.462 | -0.461 | -0.476 |
| $LiNO_3$ | -0.523 | -0.523 | -0.349 | |
| $KNO_3$ | -0.511 | -0.511 | -0.403 | |
| $NO_3^-$ | -0.475 | -0.475 | -0.475 | |
| $CH_3OK$ | -0.777 | | | |
| $CH_3OLi$ | -0.837 | | | |
| $CH_3O^-$ | -0.805 | | | |
| DME | -0.341 | -0.341 | | |
| $DME\text{-}Li^+$ | -0.472 | -0.472 | | |
| DOL | -0.359 | -0.343 | | |

**Table S2.** Summary and comparison of the cycling stability of Li|Li symmetric cells in modified electrolyte with previously reported results.

| | Current density (mA $cm^{-2}$) | Capacity (mAh $cm^{-2}$) | Cyclic stability (h) | Base electrolytes | Ref |
|---|---|---|---|---|---|
| $Al_2O_3$-$OOC(CH_2)_2COOH$-coated separator | 1 | 1 | 2500 | 1 M LiTFSI in DOL and DME (1:1 by volume) with 1 wt% $LiNO_3$ additive | [19] |
| Lithiophilic montmorillonite additive | 1 | 1 | 1200 | 1 M LiTFSI in DOL and DME (1:1 by volume) with 1 wt% $LiNO_3$ additive | [20] |
| A cation-tethered flowable polymeric interface | 1 | 1 | 1000 | 1 M LiTFSI in DOL and DME (1:1 by volume) with 1 wt% $LiNO_3$ additive | [21] |
| Polycyclic aromatic hydrocarbons artificial hybrid layer | 0.5 | 1 | 2000 | 1 M LiTFSI in DOL and DME (1:1 by volume) with 1 wt% $LiNO_3$ additive | [22] |
| $Li_4Ti_5O_{12}$ artificial layer | 1 | 1 | 1000 | 1 M LiTFSI in DOL and DME (1:1 by volume) with 2 wt% $LiNO_3$ additive | [23] |
| AgLiF-$Li_3N$ rich interface layer | 1 | 1 | 2000 | 1 M LiTFSI in DOL and DME (1:1 by volume) with 2 wt% $LiNO_3$ additive and 0.03M AgTFSI | [24] |
| LiI–LiF-rich artificial SEI layer | 1 | 1 | 300 | 1 M LiTFSI in DOL and DME (1:1 by volume) with 2 wt% $LiNO_3$ additive | [25] |
| Ag coating laye | 1 | 1 | 900 | 1 M LiTFSI in DOL and DME (1:1 by volume) with 1 wt% $LiNO_3$ additive | [26] |
| LiPEO-UPy artificial SEI layer | 1 | 1 | 2000 | 1 M LiTFSI in DOL and DME (1:1 by volume) with 2 wt% $LiNO_3$ additive | [27] |
| $Li_2S$/$Li_2Se$ coating layer | 1 | 1 | 720 | 1 M LiTFSI in DOL and DME (1:1 by volume) with 2 wt% $LiNO_3$ additive | [28] |
| Nafion/Al-doped $Li_{6.75}La_3Zr_{1.75}Ta_{0.25}O_{12}$ coating layer | 1 | 1 | 300 | 1 M LiTFSI in DOL and DME (1:1 by volume) with 2 wt% $LiNO_3$ additive | [29] |
| $C_3N_4$ artificial SEI layer | 1 | 1 | 233 | 1 M LiTFSI in DOL and DME (1:1 by volume) with 5 wt% $LiNO_3$ additive | [30] |
| Pyridine moieties additive | 0.5 | 1 | 350 | 1 M LiTFSI in DOL and DME (1:1 by volume) with 2 wt% $LiNO_3$ additive | [31] |
| 1,3,5-benzentrithiol additive | 1 | 1 | 275 | 1 M LiTFSI in DOL and DME | [32] |

| | | | | | |
|---|---|---|---|---|---|
| | | | | (1:1 by volume) with 0.15M $LiNO_3$ additive | |
| Sulfurized SEI | 1 | 1 | 500 | 1 M LiTFSI in DOL and DME (1:1 by volume) with 5 wt% $LiNO_3$ and 0.02 M $Li_2S_5$ additive | [33] |
| $Li_xSi$ coating layer | 1 | 1 | 400 | 1 M LiTFSI in DOL and DME (1:1 by volume) with 0.1M $LiNO_3$ | [34] |
| Methoxide additives | 0.5 | 0.5 | 5000 | 1 M LiTFSI in DOL and DME (1:1 by volume) with 2 wt% $LiNO_3$ | This work |
| Methoxide additives | 1 | 1 | 3500 | 1 M LiTFSI in DOL and DME (1:1 by volume) with 2 wt% $LiNO_3$ | This work |

**Table S3.** Comparison of the electrode potential (V) *vs*. standard hydrogen electrode (SHE) for various alkali metal ions with various concentrations.

| $A^+/A$ | Concentration (M) | Potential (V) *vs*. standard hydrogen electrode (SHE) |
|---|---|---|
| $K^+/K$ | 0.04 | -3.000 |
| $K^+/K$ | 1 | -2.920 |
| $Cs^+/Cs$ | 0.04 | -3.109 |
| $Cs^+/Cs$ | 1 | -3.026 |
| $Rb^+/Rb$ | 0.04 | -3.063 |
| $Rb^+/Rb$ | 1 | -2.980 |
| $Li^+/Li$ | 1.4 | -3.031 |
| $Li^+/Li$ | 1 | -3.040 |

**Notes:** The electrode potential of $Rb^+/Rb$ (0.04 M), $Cs^+/Cs$ (0.04 M), $K^+/K$ (0.04 M), and $Li^+/Li$ (1.4 M) are calculated and compared according to the following equation: [35, 36]

$$\triangle E(A^+(x\ M)/A = \triangle E\varphi(A^+/A) + 0.0592*\log(x/1)$$

Where A represents the specific alkali metal (e.g., Li, Na, K, Cs, Rb) and "x" represents the concentration of the specific alkali metal ions.

As can be seen from Table S7, the potential of $K^+/K$ vs. SHE is -3.000 V with a concentration of 0.04 M, much larger than that of $Li^+/Li$ vs. SHE (-3.040 V and -3.031 V with concentrations of 1.0 and 1.4 M, respectively), indicating no electrostatic shield effect in our electrolyte. On the contrary, the potential of $Cs^+/Cs$ and $Rb^+/Rb$ vs. SHE is much lower than -3.040 V, demonstrating $CH_3OCs$ or $CH_3ORb$ could lead to an even better result with the help of electrostatic shield effect.

**Table S4.** Summary of the calculated $E_a$ values before cycling

| | Blank electrolyte | Modified electrolyte |
|---|---|---|
| $E_{a,ct}$ (kJ/mol) | 48.8 | 39.3 |
| $E_{a,SEI}$ (kJ/mol) | 64.8 | 63.2 |

**Table S5.** Summary of the calculated $E_a$ values after cycling

| | Blank electrolyte | Modified electrolyte |
|---|---|---|
| $E_{a,ct}$ (kJ/mol) | 48.4 | 37.6 |
| $E_{a,SEI}$ (kJ/mol) | 60.2 | 53.7 |

**Table S6.** Corresponding values of $R_{ct}$ and $R_{sei}$ under various temperatures for the modified electrolyte before and after cycling.

| T (K) | $R_{ct}$ (Ω) (after / before cycling) | $R_{sei}$ (Ω) (after / before cycling) |
|---|---|---|
| 303 | 10.73 / 18.53 | 9.745 / 38.69 |
| 298 | 13.12 / 24.17 | 12.2 / 61.9 |
| 293 | 16.77 / 32.2 | 17.69 / 98.39 |
| 288 | 21.73 / 43.31 | 25.98 / 156.8 |
| 283 | 28.79 / 59.47 | 38.43 / 255.5 |
| 278 | 39.65 / 82.74 | 60.28 / 415 |
| 273 | 54.92 / 95.8 | 98.65 / 578.9 |

**Table S7.** Corresponding values of $R_{ct}$ and $R_{sei}$ under various temperatures for the blank electrolyte.

| T (K) | $R_{ct}$ (Ω) (after / before cycling) | $R_{sei}$ (Ω) (after / before cycling) |
|---|---|---|
| 303 | 17.28 / 20.5 | 22.01 / 43.63 |
| 298 | 22.95 / 26.68 | 34.56 / 73.51 |
| 293 | 31.7 / 35.35 | 42.58 / 118.3 |
| 288 | 43.87 / 49.5 | 73.44 / 192.1 |
| 283 | 62.71 / 73.51 | 116 / 315 |
| 278 | 97.04 / 112.4 | 185.1 / 513 |
| 273 | 139.7 / 143.4 | 304.9 / 705.3 |

## References


1 G. Herzog, W. Moujahid, J. Strutwolf, D. W. M. Arrigan, *Analyst* 2009, **134,** 1608-1613.
2 Plimpton, S., *J. Comput. Phys.* 1995, **117,** 1-19.
3 A. P. Thompson, H. M. Aktulga, R. Berger, D. S. Bolintineanu, W. M. Brown, P. S. Crozier, P. J. in 't Veld, A. Kohlmeyer, S. G. Moore, T. D. Nguyen, R. Shan, M. J. Stevens, J. Tranchida, C. Trott, S. J. Plimpton, J., *Comput. Phys. Commun.* 2022, **271,** 108171.
4 Sun, H., *J. Phys. Chem. B* 1998, **102,** 7338-7364.
5 H. Sun, Z. Jin, C. Yang, R. L. C. Akkermans, S. H. Robertson, N. A. Spenley, S. Miller, S. M. Todd, *J. Mol. Model.* **2016,** *22*, 47.
6 B. Shi, S. Sinha, V. K. Dhir, *J. Chem. Phys.* 2006, **124,** 204715.
7 R. E. Isele-Holder, W. Mitchell, A. E. Ismail, *J. Chem. Phys.* 2012, **137,** 174107.
8 G. S. Larsen, P. Lin, K. E. Hart, C. M. Colina, *Macromolecules* 2011, **44,** 6944-6951.
9 Gaussian 16, Revision B.01, Frisch, M.J., Trucks, G.W., Schlegel, H.B., Scuseria, G.E., Robb, M.A., Cheeseman, J.R.; Scalmani, G.; Barone, V.; Petersson, G.A.; Nakatsuji, H.; Li, X.; Caricato, M.; Marenich, A.V.; Bloino, J., Janesko, B.G., Gomperts, R., Mennucci, B., Hratchian, H.P., Ortiz, J.V., Izmaylov, A.F., Sonnenberg, J.L., Williams-Young, D., Ding, F., Lipparini, F., Egidi, F., Goings, J., Peng, B., Petrone, A., Henderson, T., Ranasinghe, D., Zakrzewski, V.G., Gao, J., Rega, N., Zheng, G., Liang, W., Hada, M., Ehara, M., Toyota, K., Fukuda, R., Hasegawa, J., Ishida, M., Nakajima, T., Honda, Y., Kitao, O., Nakai, H., Vreven, T., Throssell, K., Montgomery Jr., J.A., Peralta, J.E., Ogliaro, F., Bearpark, M.J., Heyd, J.J., Brothers, E.N., Kudin, K.N., Staroverov, V.N., Keith, T.A., Kobayashi, R., Normand, J., Raghavachari, K., Rendell, A.P., Burant, J.C., Iyengar, S.S., Tomasi, J., Cossi, M., Millam, J.M., Klene, M., Adamo, C., Cammi, R., Ochterski, J.W., Martin, R.L., Morokuma, K., Farkas, O., Foresman, J.B., Fox, D.J. Gaussian, Inc., Wallingford CT (2016) GaussView 5.0. Wallingford, E.U.A.
10 C. Lee, W. Yang and R. G. Parr, Physical Review B, 1988, **37**, 785-789.
11 F. Weigend and R. Ahlrichs, *Physical Chemistry Chemical Physics*, 2005, **7**, 3297-3305.
12 A. V. Marenich, C. J. Cramer and D. G. Truhlar, *The Journal of Physical Chemistry B*, 2009, **113**, 6378-6396.
13 C. de la Cruz, A. Molina, N. Patil, E. Ventosa, R. Marcilla and A. Mavrandonakis, *Sustainable Energy & Fuels*, 2020, **4**, 5513-5521.
14 S. Grimme, J. Antony, S. Ehrlich and H. Krieg, *The Journal of chemical physics*, 2010, **132**, 154104.
15 J. Meng, M. Lei, C. Lai, Q. Wu, Y. Liu and C. Li, *Angew Chem Int Ed Engl*, 2021, **60**, 23256-23266.
16 Y. Liu, D. Lin, P. Y. Yuen, K. Liu, J. Xie, R. H. Dauskardt and Y. Cui, *Advanced Materials*, 2017, **29**, 1605531.
17 C. Yan, X.-B. Cheng, Y.-X. Yao, X. Shen, B.-Q. Li, W.-J. Li, R. Zhang, J.-Q. Huang, H. Li and Q. Zhang, *Advanced Materials*, 2018, **30**, 1804461.
18 Z. Han, C. Zhang, Q. Lin, Y. Zhang, Y. Deng, J. Han, D. Wu, F. Kang, Q.-H. Yang and W. Lv, *Small Methods*, 2021, **5**, 2001035.
19 Y. Liu, X. Tao, Y. Wang, C. Jiang, C. Ma, O. Sheng, G. Lu, X. W. Lou, *Science* 2022, **375,** 739-745.
20 W. Chen, Y. Hu, W. Lv, T. Lei, X. Wang, Z. Li, M. Zhang, J. Huang, X. Du, Y. Yan, W. He, C. Liu, M. Liao, W. Zhang, J. Xiong, C. Yan, *Nat. Commun.* 2019, **10,** 4973.
21 Z. Huang, S. Choudhury, H. Gong, Y. Cui, Z. Bao, *J. Am. Chem. Soc.* 2020, **142,** 21393-21403.
22 S. Chang, X. Jin, Q. He, T. Liu, J. Fang, Z. Shen, Z. Li, S. Zhang, M. Dahbi, J. Alami, K. Amine, A.-D. Li, H. Zhang, J. Lu, *Nano Lett.* 2022, **22,** 263-270.
23 X. Xiong, W. Yan, Y. Zhu, L. Liu, L. Fu, Y. Chen, N. Yu, Y. Wu, B. Wang, R. Xiao, *Adv. Energy Mater.* 2022, **12,** 2103112.
24 B. Zhong, J. Wu, L. Ren, T. Zhou, Z. Zhang, W. Liu, H. Zhou, *Energy Storage Mater.* 2022, **50,** 792-801.
25 C. M. Efaw, B. Lu, Y. Lin, G. M. Pawar, P. R. Chinnam, M. F. Hurley, E. J. Dufek, Y. S. Meng, B. Li, *Mater. Today* **49**, 48-58 (2021).
26 F. Guo, C. Wu, H. Chen, F. Zhong, X. Ai, H. Yang, J. Qian, *Energy Storage Mater.* 2020, **24,** 635-643.
27 G. Wang, C. Chen, Y. Chen, X. Kang, C. Yang, F. Wang, Y. Liu, X. Xiong, *Angew. Chem. Int. Ed.* 2020, **59,** 2055-2060.
28 F. Liu, L. Wang, Z. Zhang, P. Shi, Y. Feng, Y. Yao, S. Ye, H. Wang, X. Wu, Y. Yu, *Adv. Funct. Mater.* 2020, **30,** 2001607.
29 R. Xu, Y. Xiao, R. Zhang, X. B. Cheng, C. Z. Zhao, X. Q. Zhang, C. Yan, Q. Zhang, J. Q. Huang, *Adv. Mater.* 2019, **31,** 1808392.
30 Y. Guo, P. Niu, Y. Liu, Y. Ouyang, D. Li, T. Zhai, H. Li, Y. Cui, *Adv. Mater.* 2019, **31,** 1900342.
31 T. Zhou, Y. Zhao, M. El Kazzi, J. W. Choi, A. Coskun, *ACS Energy Lett.* 2021, **6,** 1711-1718.
32 W. Guo, W. Zhang, Y. Si, D. Wang, Y. Fu, A. Manthiram, *Nat. Commun.* 2021, **12,** 3031.
33 X.-B. Cheng, C. Yan, H.-J. Peng, J.-Q. Huang, S.-T. Yang, Q. Zhang, *Energy Storage Mater.* 2018, **10,** 199-205.
34 W. Tang, X. Yin, S. Kang, Z. Chen, B. Tian, S. L. Teo, X. Wang, X. Chi, K. P. Loh, H. W. Lee, G. W. Zheng, *Adv. Mater.* 2018, **30,** 1801745.
35 X. Yang, Q. Sun, C. Zhao, X. Gao, K. Adair, Y. Zhao, J. Luo, X. Lin, J. Liang, H. Huang, L. Zhang, S. Lu, R. Li and X. Sun, *Energy Storage Materials*, 2019, **22**, 194-199.
36 F. Ding, W. Xu, G. L. Graff, J. Zhang, M. L. Sushko, X. Chen, Y. Shao, M. H. Engelhard, Z. Nie, J. Xiao, X. Liu, P. V. Sushko, J. Liu and J.-G. Zhang, *Journal of the American Chemical Society*, 2013, **135**, 4450-4456.